



Signal Enhancement of Low Magnetic Field Magnetic Resonance Image Using a Conventional- and Cyclic-Generative Adversarial Network Models With Unpaired Image Sets

OPEN ACCESS

Edited by:

Jason W. Sohn,
Allegheny Health Network,
United States

Reviewed by:

Min-Sig Hwang,
University of Pittsburgh
Medical Center,
United States

Bilgin Kadri Aribas,
Bülent Ecevit University,
Turkey

*Correspondence:

Eun Ho Kim
eunhokim8@gmail.com

Specialty section:

This article was submitted to
Radiation Oncology,
a section of the journal
Frontiers in Oncology

Received: 29 January 2021

Accepted: 08 April 2021

Published: 11 May 2021

Citation:

Yoo D, Choi YA, Rah CJ, Lee E, Cai J,
Min BJ and Kim EH (2021) Signal
Enhancement of Low Magnetic Field
Magnetic Resonance Image Using a
Conventional- and Cyclic-Generative
Adversarial Network Models With
Unpaired Image Sets.
Front. Oncol. 11:660284.
doi: 10.3389/fonc.2021.660284

Denis Yoo¹, Yuni Annette Choi¹, C. J. Rah¹, Eric Lee¹, Jing Cai², Byung Jun Min³
and Eun Ho Kim^{4*}

¹ Artificial Intelligence Research Lab, Talos, Sheung Wan, Hong Kong, ² Department of Health Technology & Informatics, Hong Kong Polytechnic University, Hung Hom, Hong Kong, ³ Department of Radiation Oncology, Chungbuk National University Hospital, Cheongju, South Korea, ⁴ Department of Biochemistry, School of Medicine, Daegu Catholic University, Daegu, South Korea

In this study, the signal enhancement ratio of low-field magnetic resonance (MR) images was investigated using a deep learning-based algorithm. Unpaired image sets (0.06 **Tesla** and 1.5 **Tesla** MR images for different patients) were used in this study following three steps **workflow**. In the first step, the deformable registration of a 1.5 **Tesla** MR image into a 0.06 **Tesla** MR image was performed to ensure that the shapes of the unpaired set matched. In the second step, a cyclic-generative adversarial network (GAN) was used to generate a synthetic MR image of the original 0.06 **Tesla** MR image based on the deformed or original 1.5 **Tesla** MR image. Finally, an enhanced 0.06 **Tesla** MR image could be generated using the conventional-GAN with the deformed or synthetic MR image. The results from the optimized flow and enhanced MR images showed significant signal enhancement of the anatomical view, especially in the nasal septum, inferior nasal concha, nasopharyngeal fossa, and eye lens. The signal enhancement ratio, signal-to-noise ratio (SNR) and correlation factor between the original and enhanced MR images were analyzed **for the evaluation of the image quality**. A combined method using conventional- and cyclic-GANs is a promising approach for generating enhanced MR images from low-magnetic-field MR.

Keywords: conventional-GAN, cyclic-GAN, enhancement of MR image, low magnetic field, Magnetic Resonance Image (MRI)

INTRODUCTION

Magnetic resonance imaging (MRI)-based contouring is a standard practice in radiotherapy (1–4). Recently, the use of MRI has been extended to the entire external photon radiotherapy (RT) treatment planning workflow (5–16). In addition, for proton therapy, the feasibility of magnetic resonance (MR)-only treatment planning has been investigated (17, 18). In this MR-only RT workflow, the development of techniques for determining the electron density in MRI-derived substitute-computed tomography (sCT) images have been investigated, including atlas-based and deep learning-based methods (18–22). For synthetic CT generation, Han's generative adversarial network (GAN) model (20) or modified models (18, 21, 22) have generally been used with sets of two-paired images (an MR/CT image set for the same patient taken within one day). In this conventional GAN, the CT images are the ground truth, and the MR images are the input images.

In addition to sCT, the generation of synthetic MRI for image-to-image translation of T1- and T2-weighted MR images (23) has been investigated using a cyclic-GAN algorithm. The neural network training is commonly supervised, that is, the training requires the corresponding ground truth for each input sample. In image-to-image translation, this implies that paired images from both the source and target domains are needed. To alleviate this constraint, the cyclic-GAN (24) and UNIT (25) can work with unpaired training data. In this cyclic-GAN, two input images tend to resemble each other.

1.5 Tesla has become the standard clinical machine even in very small hospitals, almost completely replacing the older lower field strength (0.2–1 Tesla) machines that played an important role in the development of MRI during the 1980s (26). Recent advances in MRI technology have allowed for data acquisition at low magnetic field strengths. MRI scanners operating at low field strengths allow for open geometry designs that can ease patient handling and positioning and are compatible with nearby ferromagnetic materials, enabling scanning outside of the controlled access environment of an MRI suite (27). Sheth et al., recently developed and deployed a novel bedside neuroimaging solution and reported the results (28). They used a 0.06 Tesla portable MR (hyperfine MR) machine for the assessment of brain injury. This portable MR machine was very efficient, especially for patients admitted to an intensive care unit. Though this technology is very promising, improvement of the image quality is necessary to apply this MRI to a more wide area; and to increase the image quality, a deep learning model can be a useful option.

To generate sCT from MR images, the image quality of the MRI must be assured, however, the current situation of the low magnetic field-based MR images were not of the quality required for the sCT generation. Thus, the quality of MRI from low-magnetic-field MR needs to be improved for the clinical usage of the MR-only RT workflow. Also, paired image sets for the training of the deep learning algorithm are not suitable in some clinical situations. However, the study of deep learning model-based training with unpaired image set has not been fully

investigated yet. This study investigated the MR signal enhancement of 0.06 Tesla MRI using deep learning-based combined models (cyclic-GAN and conventional-GAN) with unpaired image sets. We suggested a clinical workflow using deformable registration and a deep learning-based combined model consisting of cyclic- and conventional-GAN. Also, three kinds of methods were compared to find an optimal workflow for the enhancement of the MR images.

METHOD

Patient Data and Matching Unpaired Image Set

This study used axial 0.06 Tesla MR images from the Hyperfine website (<https://hyperfine.io/clinical>) with 26 images for T1-weighted (T1W) used for training and evaluation. In addition, 1.5 Tesla MR images from another website (<http://www.med.harvard.edu/aanlib/home.htm>) were used as reference images with the same number of slices. These unpaired images were matched to each other by a radiologist to ensure that they were as similar as possible. **Figure 1** shows an unpaired image set containing a 0.06 Tesla original MR image and 1.5 Tesla original MR image. For all the images, an image size of 256×256 and depth of 255 (8 bit) was used. The detailed imaging parameters for the 0.06 Tesla MRI are shown in (28). 0.06 Tesla MR images were acquired using an 8-channel head coil. The MRI used a biplanar, 3-axis gradient system with a peak amplitude of 26 mT/m (on the z-axis) and 25 mT/m (on the x-axis and y-axis). The scanning parameters were controlled using a computer interface (iPad Pro, third-generation; Apple). The following pulse 3-dimensional sequences were used: T1W fast spin echo (FSE) (repetition time [TR], 1500 milliseconds; time to echo [TE], 6 milliseconds; inversion time [TI], 300 milliseconds; $1.5 \times 1.5 \times 5$ -mm resolution; 36 slices). Examinations were acquired in the axial, sagittal, and coronal planes. In this study, the main aim is to study the enhancement of the brain structure in MRI, thus normal whole-brain images were used for both 0.06 and 1.5 Tesla MR images.

In hyperfine MRI (0.06 Tesla MRI), the overall intensity is low compared to 1.5 Tesla MRI, and the eye lens and nasal structure were not visible. The slices had different shapes in the 0.06 Tesla and 1.5 Tesla images, as well as different positions sizes. In this study, cyclic-GAN with and without deformable registration was applied to investigate the match of the unpaired image set. The detailed workflow and methods are presented in the next section.

Workflow

This study suggested a three-step clinical flow for generating enhanced MR images using 0.06 Tesla MRI, as shown in **Figure 2**. In the first step, a deformable registration process was used to match different positions and sizes of the unpaired MR image set (0.06 Tesla MR and 1.5 Tesla MR). A midpoint independent deformable registration method (29) was applied to deform a 1.5 Tesla MR image based on 0.06 Tesla MR image. In the second step, a cyclic-GAN was applied to generate a synthetic MR images from the deformed or original 1.5 Tesla MR image.

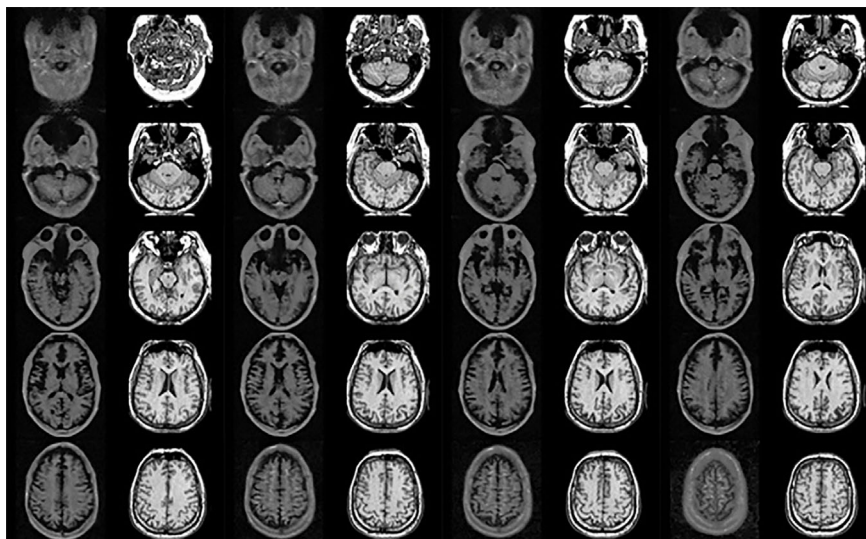


FIGURE 1 | Unpaired image set used for training (left and right sides show 0.06 Tesla and 1.5 Tesla MR images, respectively).

Clinical Workflow for MRI signal enhancement

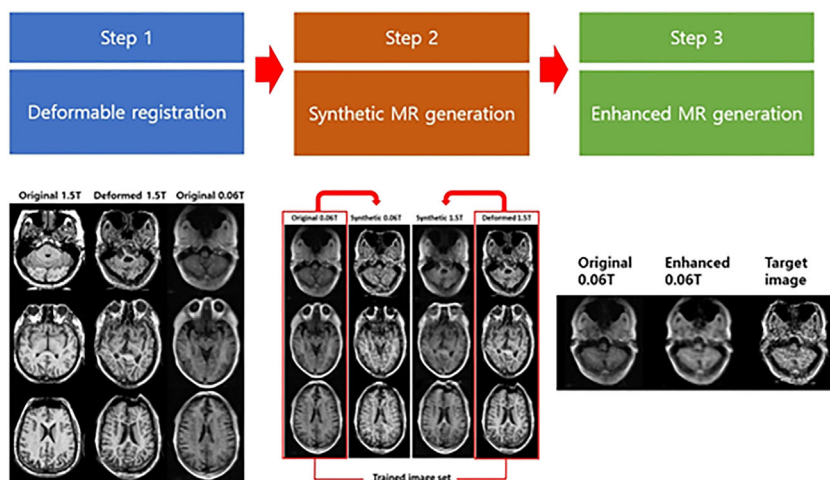


FIGURE 2 | Clinical flow for enhancement of unpaired MRI set.

This synthetic MR image was then used as a reference image in the third step to generate enhanced MRI.

To investigate the qualities of the enhanced MRI, three methods (methods 1, 2 and 3) were used with the clinical flow. In method 1, an enhanced MR image was generated from the original 0.06 Tesla MR image using the deformable registration and conventional-GAN model (without the cyclic-GAN model). We prepared training image sets with unpaired 0.06 and 1.5 Tesla MR images in each slice. Then, deformable registration was applied in the unpaired image sets. In each step, an experienced clinical physicist reviewed the process and registration results.

In method 2, the deformed 1.5 Tesla MR image (after deformable registration) and original 0.06 Tesla MR image were used as the input/reference images for the synthetic MRI generation in the cyclic-GAN. At this stage, there were two synthetic images—one was a synthetic MR image (from the original 0.06 Tesla MR image) that resembled the deformed 1.5 Tesla MR image, and the other was a synthetic MR image (from the deformed 1.5 Tesla MR image) that resembled the original 0.06 Tesla MR image. Among them, the synthetic MR image from the original 0.06 Tesla MR image was used as the reference image in the conventional-GAN model.

In method 3, the original 1.5 Tesla MR image (without deformable registration) and original 0.06 Tesla MR image were used as input/reference images for the synthetic MRI generation in the cyclic-GAN. Then, the synthetic MR image from the original 0.06 Tesla MR image (which resembled the original 1.5 Tesla MR image) was used as the reference image in the conventional-GAN model.

Table 1 shows the clinical flow and the three methods to enhance the MR images with deformable registration, cyclic-GAN, and conventional-GAN deep learning models.

The software system for deep learning algorithm includes Python 3.7.7, TensorFlow 2.3.1, NumPy 1.18.5, OpenCV 4.4.0, Matplotlib 2.2.3, pickleshare 0.7.5, SimpleITK 2.0.1, SciPy 1.1.0, and CUDA 11.0 with a Nvidia 12 GB Titan X GPU.

Training and Evaluation for Conventional-GAN (Step 2) and Cyclic-GAN (Step 3)

This study used a training set of 26 slices of T1W unpaired image set. For the 2nd step, a cyclic-GAN model (23) (<https://github.com/simontomaskarlsson/GAN-MRI>) was used to generate synthetic MR images using the 0.06 Tesla MR and 1.5 Tesla MR images. The training set was used for a test because the aim of this study was to determine the feasibility of using the enhanced MRI signals from the 0.06 Tesla MRI. The evaluation process of the algorithm is presented in (23). The training process was performed with the original 0.06 Tesla MR image and deformed 1.5 Tesla MR image (method 2) or original 1.5 Tesla MR image (method 3), as shown in **Table 1**. The training of neural networks is commonly supervised, that is, the training requires the corresponding ground truth for each input sample. In image-to-image translation, this implies that paired images

from both the source and target domains are needed. To alleviate this constraint, a cyclic-GAN can work with unpaired training data. In the training, 180 epochs were used and six model comparisons were conducted.

In the 3rd step, the training process was performed with the reference image of the generated synthetic MRI from the 0.06 Tesla MR image with the 1.5 Tesla MR image (deformed or original) and the input image of the original 0.06 Tesla MR image. Han’s model (20) was used for the conventional-GAN in the 3rd step (<https://github.com/ChengBinJin/MRI-to-CT-DCNN-TensorFlow>). In previous work on synthetic CT generation from MR images (18, 20–22), preprocessing of the CT and MR image sets was needed. In these previous studies, after preprocessing, the input image (original CT) and reference image (original MR) were converted to resampled CT images and mark out MR images that were used for training for synthetic CT image generation. However, this study used MR images for both the input and output. If a preprocessing algorithm was used for the image set, the intensity of the 0.06 Tesla MR image (input image) became low, as shown in **Figure 3**. Thus, the original 0.06T MR image and synthetic MR image were used without preprocessing, even though preprocessing was performed. Mask images that were generated during this preprocessing were used for loss function training and evaluation.

In the conventional-GAN, the weights and biases of trainable filters in the convolutional layers and deconvolutional layers were trained by minimizing a loss function. The loss function was defined as the mean absolute error (MAE) between OS_i and IS_i within the body mask:

$$loss = \frac{1}{N} \sum_{i=1}^N |OS_i - IS_i|,$$

TABLE 1 | Workflow with deformed MR image and without synthetic MR image for method 1, 2 and 3.

Method/Flow	Step 1		Step 2		Step 3
Method1	Model	Deformable registration		Cyclic-GAN	Conventional-GAN
	Input	Original 1.5T MR image		Not applicable	Original 0.06T MR image
	Reference	Original 0.06T MR image			Deformed 1.5T MR image
	Output	Deformed 1.5T MR image			Enhanced 0.06T MR image
Method2	Model	Deformable registration		Cyclic-GAN	Conventional-GAN
	Input	Original 1.5T MR image	Original 0.06T MR image	Deformed 1.5T MR image	Original 0.06T MR image
	Reference	Original 0.06T MR image	Deformed 1.5T MR image	Original 0.06T MR image	Synthetic MR image from 0.06T MR image with deformed 1.5T MR image
	Output	Deformed 1.5T MR image	Synthetic MR image from 0.06T MR image (used)	Synthetic MR image from deformed 1.5T MR image (not used)	Enhanced 0.06T MR image
Method3	Model	Deformable registration		Cyclic-GAN	Conventional-GAN
	Input	Not applicable	Original 0.06T MR image	Original 1.5T MR image	Original 0.06T MR image
	Reference		Original 1.5T MR image	Original 0.06T MR image	Synthetic MR image from 0.06T MR image with original 1.5T MR image
	Output		Synthetic MR image from 0.06T MR image (used)	Synthetic MR image from original 1.5T MR image (not used)	Enhanced 0.06T MR image

(0.06T and 1.5T indicate 0.06 Tesla and 1.5 Tesla respectively).

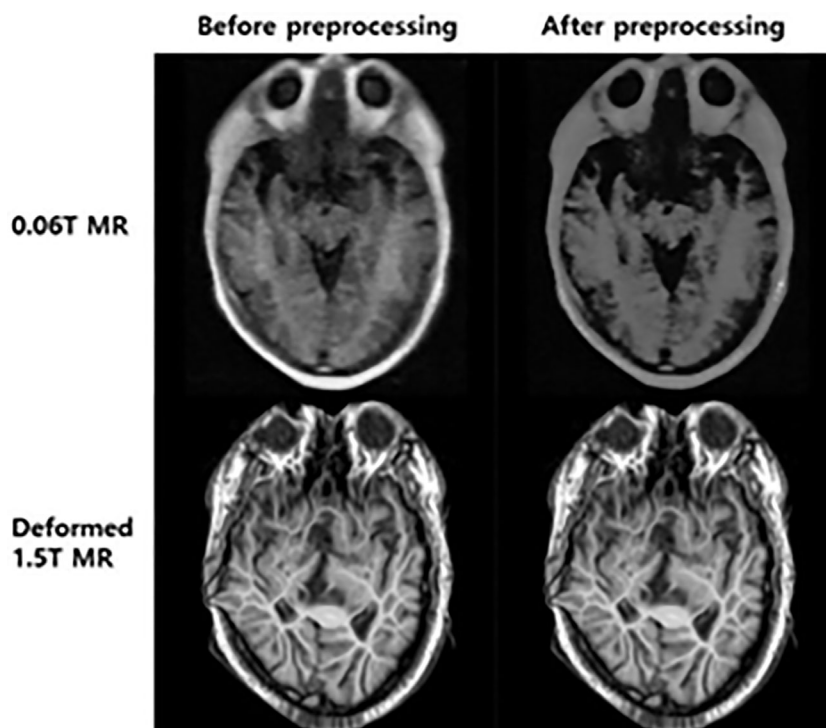


FIGURE 3 | Reduced intensity after preprocessing of MR images (Han's model).

Where N is the number of voxels inside the body masks of the MR images, and OS_i and IS_i represent the intensity values of the i th voxel in the output image and input image, respectively.

In the cyclic-GAN, the goal was to learn a mapping function between the OS and IS domains given training samples. Thus, in addition to the adversarial loss (the above equation for the MAE) to both mapping functions, the learned mapping function was checked for cyclic consistency. Each image from the domain also had to satisfy the backward cycle consistency (cycle consistency loss) (24).

For a quantitative analysis of image matching between the images in step 3, a correlation factor (f) was calculated for the deformed and synthetic images as follows:

$$f = \frac{\sum_m \sum_n (A_{mn} - \bar{A})(B_{mn} - \bar{B})}{\sqrt{(\sum_m \sum_n (A_{mn} - \bar{A})^2)(\sum_m \sum_n (B_{mn} - \bar{B})^2)}}$$

Where A and B are the two image sets being compared, $\bar{A} = \text{mean}(A)$ and $\bar{B} = \text{mean}(B)$.

To analyze the performance of the enhanced image, the enhancement ratio ($S1/S2$) and signal-to-noise (SNR) ratio of the output image based on the input image were investigated, where $S1$ and $S2$ were the average values of intensity for the input image (original 0.06T MR image) and output image (enhanced 0.06 Tesla MR image), respectively.

RESULTS

Image Matching With Deformable Registration and Synthetic MR Image Generation in Cyclic-GAN (Step 1 and 2)

Figure 4 shows an example of the deformable registration. In the 1st step, midpoint independent deformable registration was applied to the original 1.5 Tesla MR image according to the 0.06 Tesla original MR image. Because unpaired sets (from different subjects) were used in this study, the initial shapes of the two original images were quite different. After deformable registration, the outer shape of the 1.5 Tesla image matched well with the original 0.06 Tesla image; however, the internal structure broke down compared to the original structure.

In the 2nd step, two methods were used to generate the synthetic MR images. One used **deformed MR images** (method 2), and the other used **original MR images** (method 3). **Figure 5** shows the results for synthetic MR images using the original 0.06 Tesla MR image and deformed 1.5 Tesla MR image. The original 0.06 Tesla MR image and deformed 1.5 Tesla MR image were trained to resemble each other using a cyclic-GAN model. The synthetic 0.06 Tesla MR image and 1.5 Tesla MR image were generated from the original 0.06 Tesla and deformed 1.5 Tesla images, respectively. In this case, the deformed 1.5 Tesla images were matched with the original 0.06 Tesla images

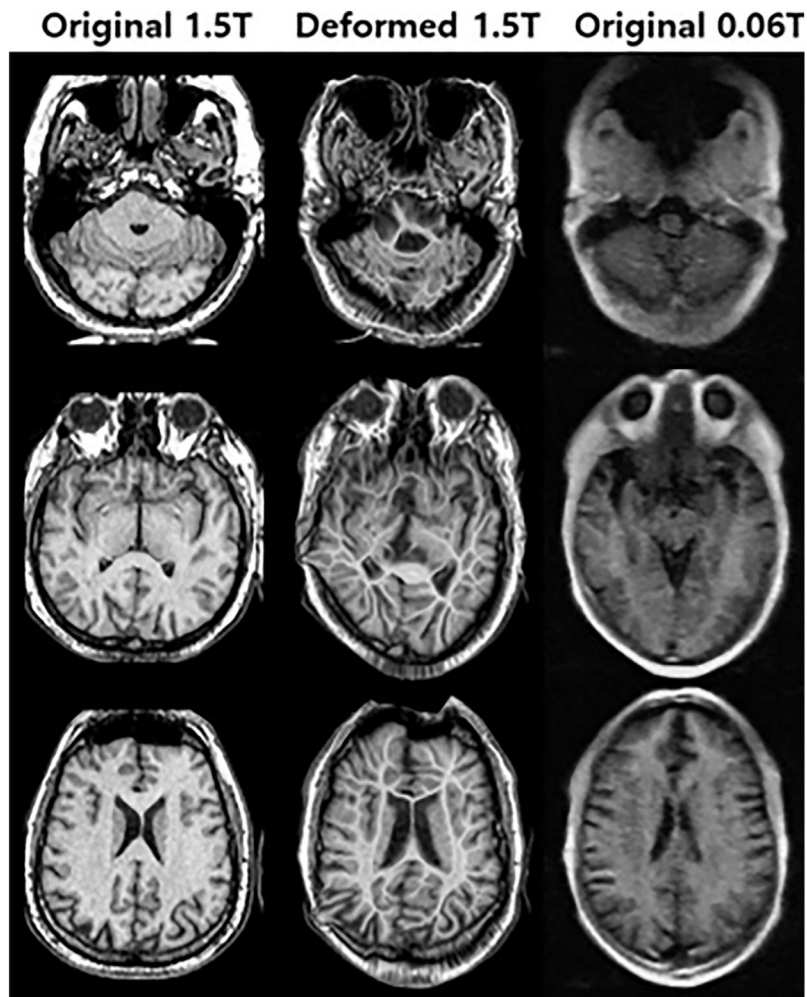


FIGURE 4 | Deformed 1.5 Tesla MR image from original 1.5 Tesla MR image according to 0.06 Tesla MR image in step 1 (deformable registration).

in relation to their sizes and positions which generated synthetic 0.06 Tesla images with sizes and positions similar in those of the original 0.06 Tesla images.

After deformable registration, some images showed poor quality as like artifact due to the distortion of the image. This is an effect of the deformation with an unpaired image set. Thus we studied method 3. In method 3, the synthetic MR images were generated from the original 0.06 Tesla and original 1.5 Tesla MR images. In this case, the synthetic 0.06 Tesla images showed a higher quality for the internal structure; however, the outer shape (position and size) was close to that of the original 1.5 Tesla. **Figure 6 shows the results for synthetic MR images using the original 0.06 Tesla MR image and the original 1.5 Tesla MR image.**

Figure 7 shows the results for the correlation factor of the deformed images (circle) and synthetic images from the deformed (square) or original images (triangle). Among the three methods, method 2 with the related synthetic MR image had the highest

correlation factor. The synthetic images from the original image (not deformed) showed the lowest correlation factor.

Enhanced MR Generation With Conventional GAN Model (Step 3)

In the final step (3rd step), deformed 1.5 Tesla and synthetic 0.06 Tesla images with the deformed 1.5 Tesla or original 0.06 Tesla MR images were used as the reference images for the generation of enhanced MR images using the conventional-GAN model. **Figures 8–10** show the results for the generated enhanced 0.06T MR image (output image) with the training set of the original 0.06 Tesla image (input image) and the various target images (reference images).

In **Figure 8**, the intensity of the nasopharyngeal fossa is enhanced compared to the original 0.06 Tesla MR image. In addition, the overall intensities of the tissue and bone are increased in the enhanced 0.06 Tesla MR image. The analytic structure of the nasopharyngeal fossa is seen more clearly in the

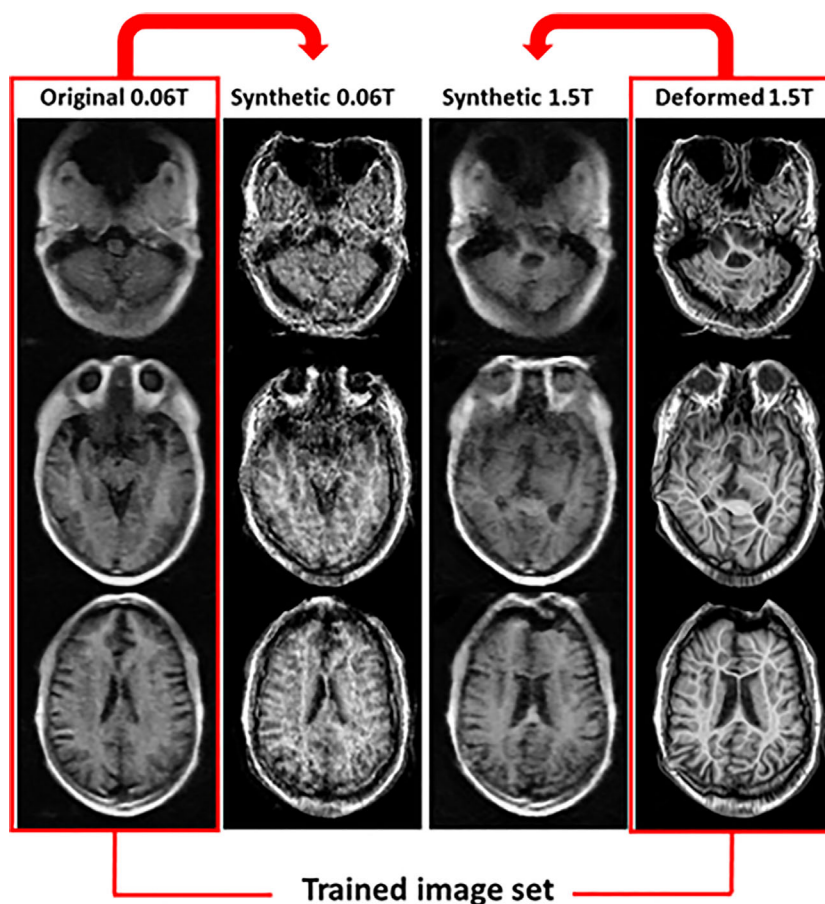


FIGURE 5 | Synthetic MR images from original 0.06 Tesla and deformed 1.5 Tesla MR images in step 2 (cyclic-GAN model, method 2).

trained image set of the deformed 1.5 Tesla image; however the overall intensity of the tissue is increased in the synthetic MR image cases.

Figure 9 shows the signal enhancement for the nasal septum and inferior nasal concha. In addition, the signal intensities were increased in the temporal lobe, medulla oblongata and cerebellar hemisphere. The analytic structure of the nasal septum was seen more clearly after using methods 2 and 3. After method 1, there was a vague pattern in the boundary between the temporal lobe and cerebellar hemisphere, including the medulla oblongata. The shape of the enhanced 0.06 Tesla MR image in method 2 was well-matched to the original 0.06 Tesla MR image. Thus, the enhanced nasal septum revealed the anatomic structure reasonably. However, in method 3, the shape was distorted because of the different shape of the original 1.5 Tesla MR image in comparison to the original 0.06 Tesla MR image.

Figure 10 shows the enhanced 0.06 Tesla MR image, especially the nasal septum, olfactory nerve, and eye lens. After using method 1, the boundary of the brainstem was unclear. The anatomical structure of the nasal septum could be seen more clearly after method 2 than method 1. In the case of method 3,

the enhanced nasal septum structure seemed abnormal compared to the result from method 2. In addition, the contrast of the overall tissue area was more palpable in method 2 than in method 1.

Figure 11 shows the results of a quantitative analysis of the enhancement of the MR images using each method. This quantitative analysis was conducted to determine the enhancement of the MR image intensity in the overall region (256×256 image size). The depth of the MR image in this study was 255 (8 bit-PNG image file). **Figure 11** shows the signal ratio of the enhanced 0.06 Tesla MR image to the original 0.06 Tesla MR image in step 3 for each method (1, 2, and 3). In **Figure 10** (A), the enhancement ratios show the ratio of the signal intensities of the enhanced MR image (S2) to that of the original MR image (S1) for method 1 (circle), method 2 (square), and method 3 (triangle). The enhancement ratios for methods 1 and 2 could increase up to 20% among slices, and the enhancement ratio for method 3 increased to approximately 50% compared to the original 0.06 Tesla MR image. **Figure 10** (B) shows the SNR of the enhanced 0.06 Tesla MR image based on the background of the original 0.06 Tesla image. The SNR values for methods 1 and 2 were higher than that of method 3.

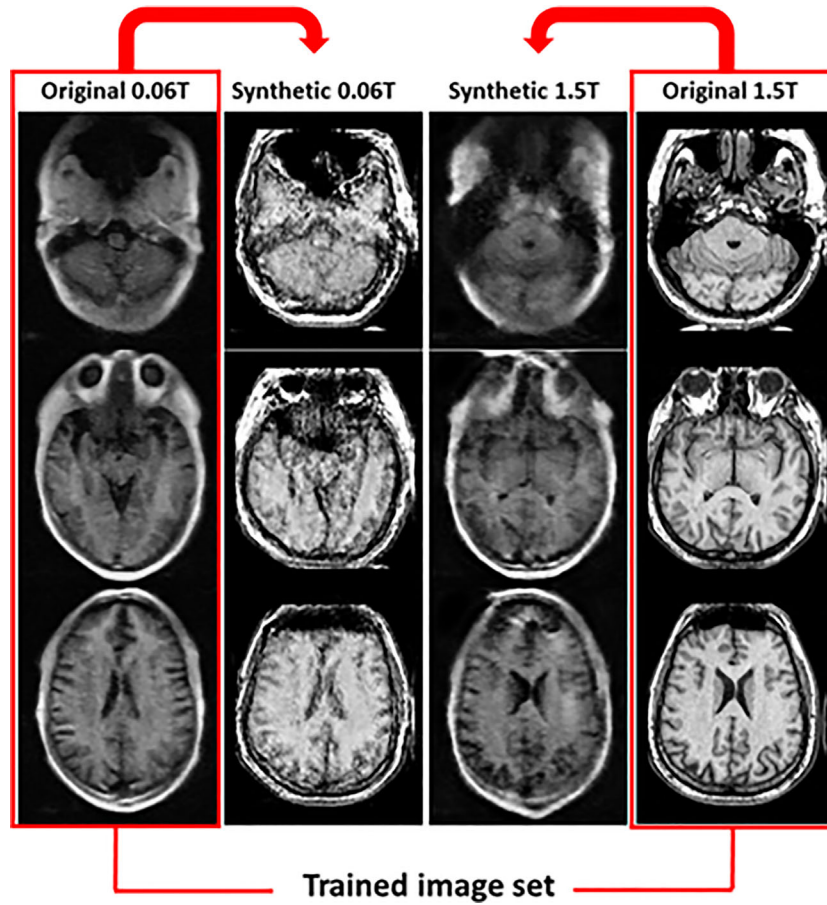


FIGURE 6 | Synthetic MR images from original 0.06 Tesla and original 1.5 Tesla MR images in step 2 (cyclic-GAN model, method 3).

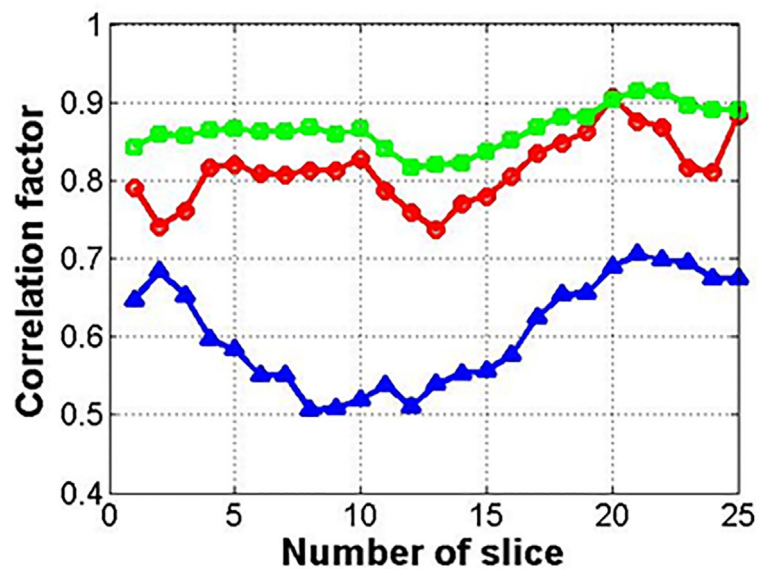


FIGURE 7 | Correlation factor between input and reference images (circle, square, and triangle marks indicate deformed image, synthetic image from deformed one, and original one, respectively).

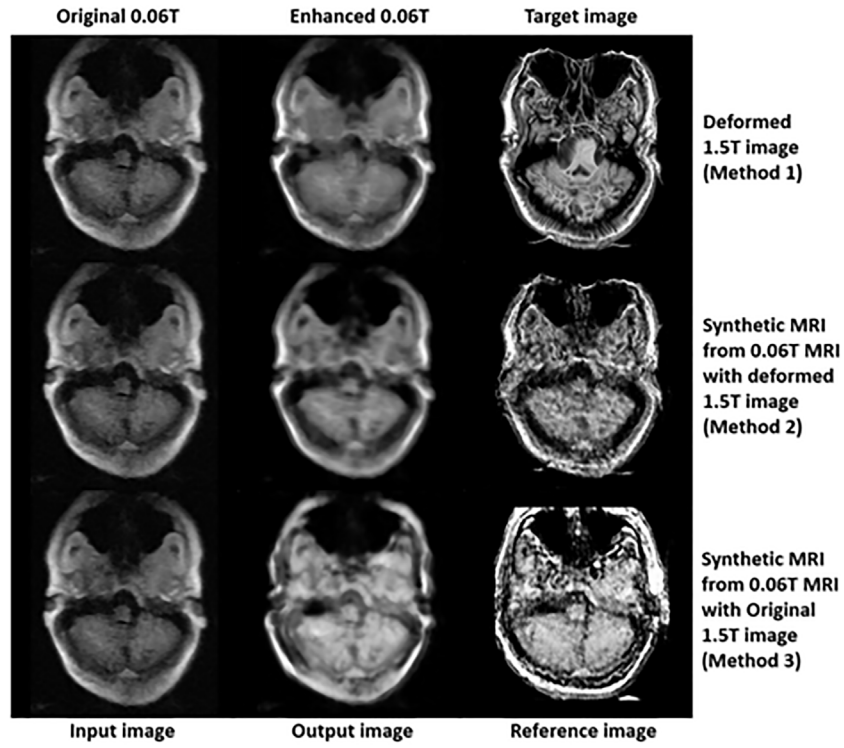


FIGURE 8 | Results of enhanced MRI of slice no. 5 in step 3 (conventional-GAN model).

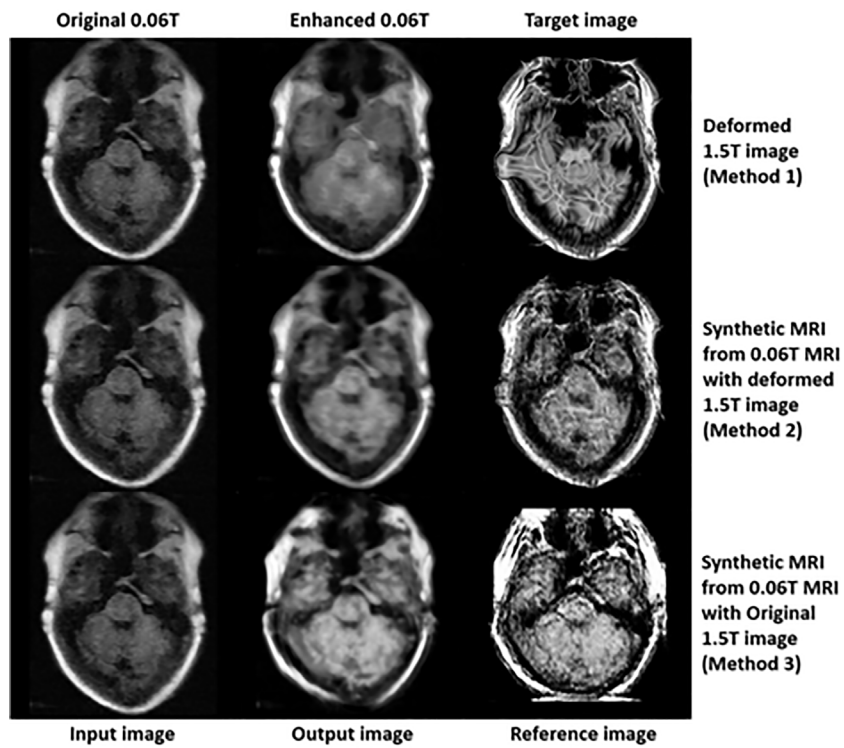


FIGURE 9 | Results of enhanced MRI of slice no. 8 in step 3 (conventional-GAN model).

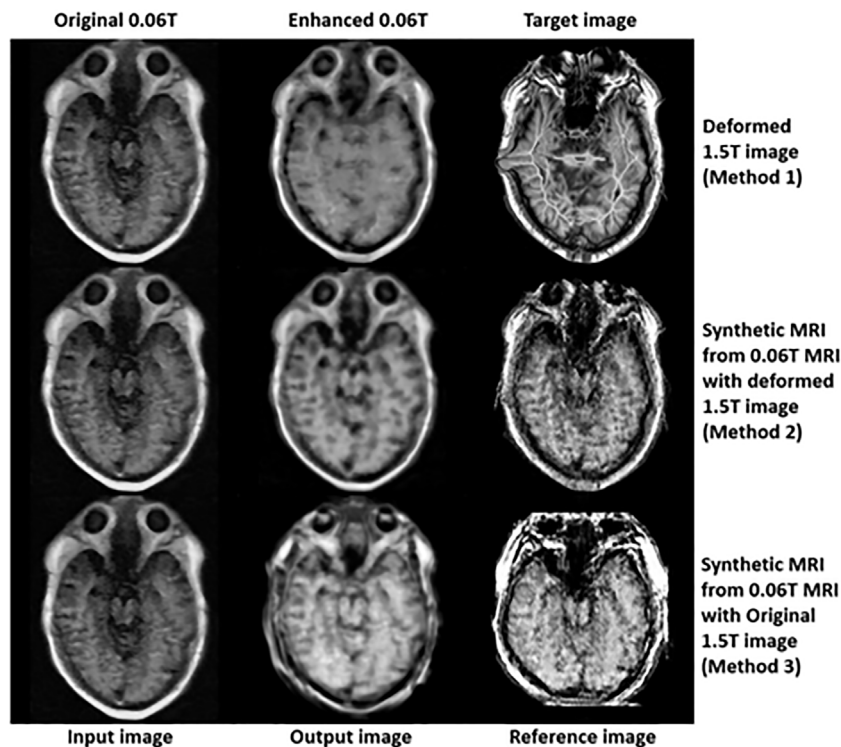


FIGURE 10 | Results of enhanced MRI of slice no. 10 in step 3 (conventional-GAN model).

Figure 12 shows the correlation factor between the input image (original 0.06 Tesla MR image) and output image (enhanced 0.06 Tesla MR image). The circle, square, and triangle marks indicate methods 1, 2, and 3, respectively. The correlations for methods 1 and 2 are higher than that for method 3. And moreover, the correlation for the enhanced image was improved compared to the reference cases in **Figure 7**.

DISCUSSION

In (23), several different GAN models were investigated in a literature study (24, 25, 30–33). And cyclic-GAN (24) and UNIT (25) were selected. The generation of synthetic images took 0.0176 and 0.0478 ms per image for the cyclic-GAN and UNIT, respectively using an Nvidia 12 GB Titan X GPU with 180 epochs. In the present study, to reduce the process time, a cyclic-GAN was selected, and the generation time was 0.0183 ms per image using the same system.

Synthetic MR images are shown in **Figures 5** and **6**. In the cyclic-GAN model, the adversarial loss had to be established for both image domains (input and reference in **Table 1**) with cyclic loss consistency (24). The synthetic MR images generated from the 0.06 Tesla and 1.5 Tesla images became close to each other. In methods 2 and 3, only the synthetic MR images from the 0.06 Tesla MR image which resembled the 1.5 Tesla MR image, were used as reference images in step 3 (conventional-GAN).

The synthetic MR images from the 1.5 Tesla MR image which was similar in the 0.06 Tesla MR image, were not used in this study.

In the case of method 1, a deformable registration process was applied. However, although this process made the shape (size and position) of the original 1.5 Tesla MR image close to that of the original 0.06 Tesla MR image, the internal anatomical structure broke down, as shown in **Figure 4**. This was due to the use of unpaired image sets between the original 0.06 Tesla and 1.5 Tesla MR images. Then, enhanced MR images were generated in step 3 through the conventional-GAN model without step 2 (synthetic MR image generation with cyclic-GAN). The shape of the enhanced MR image was close to the original 0.06 Tesla image. However, the internal structure was not as clear compared to the other methods (methods 2 and 3), as shown in **Figures 9** and **10**.

In the case of method 2, the synthetic MR image generated with the deformed 1.5 Tesla MR image showed a higher performance in terms of the shape (size and position) and internal structure than method 1. The nasal structure and border of the brainstem were seen more clearly than with method 1 (**Figures 8–10**). However, the enhancement ratio was similar to the pattern over all the slides (**Figure 11**).

To avoid the distortion of the deformed image, method 3 used the original 1.5 Tesla MR image reference image in step 3. The nasal structure and eye lens were seen the most clearly, and the enhancement ratio showed the highest value over all the slides. However, method 3 showed poor performance for the shape,

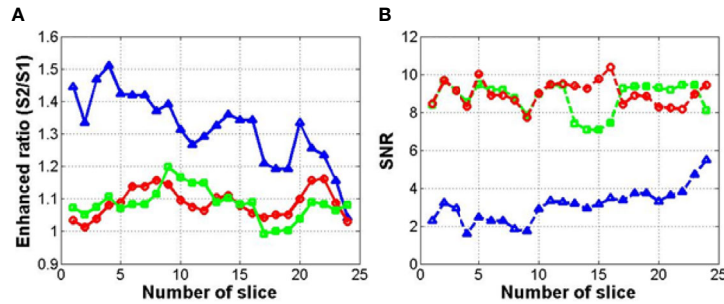


FIGURE 11 | Enhancement ratio (A) and signal-to-noise ratio (SNR) (B) of enhanced MR image for each method (circle, square, and triangle marks indicate methods 1, 2, and 3, respectively).

although it showed a relatively higher quality for the internal structure (Figures 10, 11). This could result in another distortion of the enhanced MR images, which was the limitation of using the unpaired image set.

The correlation factor indicates the resemblance between the two images—the input image and output image. In Figure 7, which shows the results after cyclic-GAN, the input and output images were the original 0.06 Tesla MR image and the deformed or synthetic images according to methods 1, 2, and 3. In Figure 12, the calculated correlation factors between the enhanced MR images and the original images are slightly higher than the results in Figure 7. However, the difference was not very significant. For the enhancement ratio, a significant difference between the input and output images was generated after the conventional-GAN, as shown in Figure 11. This implied that deformable registration and synthetic MR image

generation with the cyclic-GAN had an important role in the correlation in the workflow. Also, conventional-GAN was contributed to the signal enhancement of the MR images.

For the quantitative analysis, we calculated the correlation factor, enhancement ratio, and signal-to-noise ratio as the evaluation factors for the image quality of the enhanced MR image. These factors were compared among the three methods as shown in Table 2.

Methods 1 and 2 show almost similar evaluation factors over all items with a high correlation factor and about 10% enhancement of the MR image signal. In the case of method 3, the enhancement ratio was higher than those of methods 1 and 2 (over 30%), however, the correlation factor decreased significantly. Though the signal enhancement was superior, the image correlation between the input and output images is more important in clinical application. Also, while the evaluation factors

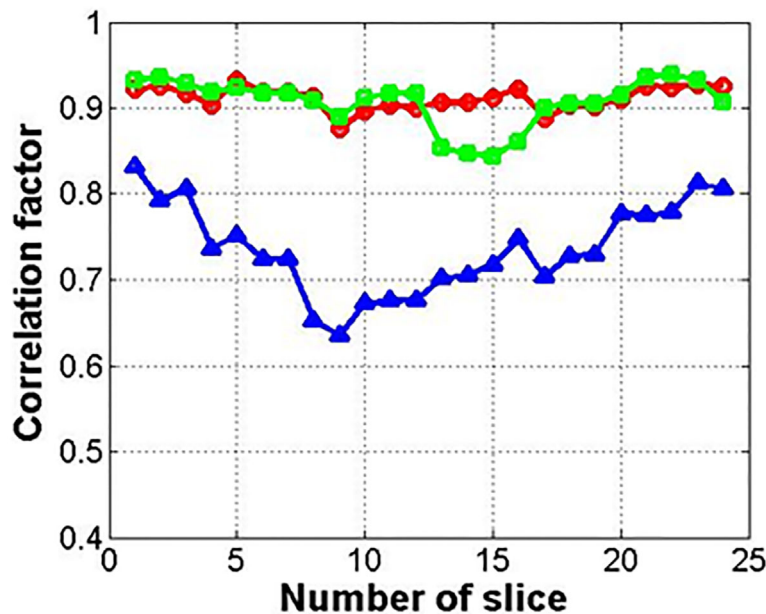


FIGURE 12 | Correlation factor between input and output images for GAN (circle, square, and triangle marks indicate methods 1, 2, and 3, respectively).

TABLE 2 | Evaluation factors of the enhanced MR images for three method.

Method/Item	Correlation Factor	Enhancement Ratio	Signal-to-Noise Ratio (SNR)
Method1	0.91±0.01	1.09±0.04	8.99±0.65
Method2	0.91±0.03	1.09±0.05	8.76±0.83
Method3	0.74±0.05	1.32±0.11	3.10±0.89

showed similar values in methods 1 and 2, the qualitative analysis showed that method 2 was the best option in this study due to its clear internal structure as compared to method 1.

In our study, we used 26 images of the unpaired image sets (26 0.06 Tesla MR images and 26 1.5 Tesla MR images). These images were used in training and evaluation. Also, the same images were used in testing for cyclic-GAN and conventional-GAN models. Thus, we do not have enough data for presenting statistical information in this study. To overcome the current limitation of our study, more data should be mined and studied further.

CONCLUSIONS

This study investigated a deep learning-based three-step workflow to increase the signal intensity for MR images and determine feasibility of generating an enhanced MR image with an unpaired image set. Deformable registration is one of the options to create a reference image from the unpaired image set in the GAN model. Synthetic images using a cyclic-GAN were suitable for the creation of a reference image of the unpaired set in the conventional-GAN model. To avoid the image distortion of the final enhanced MR image, using the synthetic deformed MR image was found to be better than using the original synthetic MR image in the cyclic-GAN. The conventional-GAN and cyclic-GAN models could be used to efficiently generate enhanced MR images in low-magnetic-

field (0.06 Tesla) MRI. To obtain the maximum efficiency, the optimized workflow (method 2 in this study) could be used for clinical purposes.

DATA AVAILABILITY STATEMENT

The raw data supporting the conclusions of this article will be made available by the authors, without undue reservation.

AUTHOR CONTRIBUTIONS

DY, YC, CR and EL conceived of the presented idea. DY and BM developed the theory and performed the computations. JC and EK verified the analytical methods. DY, YC, CR and EL encouraged EK to investigate medical efficiency and supervised the findings of this work. All authors discussed the results and contributed to the final manuscript. All authors contributed to the article and approved the submitted version.

FUNDING

This work was supported by the grant of Research Institute of Medical Science, Catholic University of Daegu (2020).

REFERENCES

1. Khoo VS, Joon DL. New Developments in MRI for Target Volume Delineation in Radiotherapy. *Br J Radiol* (2006) 79(Spec No 1):2–15. doi: 10.1259/bjr/41321492
2. Sciarra A, Barentsz J, Bjartell A, Eastham J, Hricak H, Panebianco V, et al. Advances in Magnetic Resonance Imaging: How They are Changing the Management of Prostate Cancer. *Eur Urol* (2011) 59(6):962–77. doi: 10.1016/j.eururo.2011.02.034
3. Dirix P, Haustermans K, Vandecaveye V. The Value of Magnetic Resonance Imaging for Radiotherapy Planning. *Semin Radiat Oncol* (2014) 24(3):151–9. doi: 10.1016/j.semradonc.2014.02.003
4. Seppala T, Visapaa H, Collan J, Kapanen M, Beule A, Kouri M, et al. Converting From CT- to MRI Only-Based Target Definition in Radiotherapy of Localized Prostate Cancer: A Comparison Between Two Modalities. *Strahlenther Onkol* (2015) 191(11):862–8. doi: 10.1007/s00066-015-0868-5
5. Korhonen J, Kapanen M, Keyrilainen J, Seppala T, Tenhunen M. A Dual Model HU Conversion From MRI Intensity Values Within and Outside of Bone Segment for MRI-based Radiotherapy Treatment Planning of Prostate Cancer. *Med Phys* (2014) 41(1):011704. doi: 10.1118/1.4842575
6. Korhonen J, Kapanen M, Keyrilainen J, Seppala T, Tuomikoski L, Tenhunen M. Influence of MRI-based Bone Outline Definition Errors on External Radiotherapy Dose Calculation Accuracy in Heterogeneous pseudo-CT Images of Prostate Cancer Patients. *Acta Oncol* (2014) 53(8):1100–6. doi: 10.3109/0284186X.2014.929737
7. Korhonen J, Kapanen M, Sonke JJ, Wee L, Salli E, Keyrilainen J, et al. Feasibility of MRI-based Reference Images for Image-Guided Radiotherapy of the Pelvis With Either Cone-Beam Computed Tomography or Planar Localization Images. *Acta Oncol* (2015) 54(6):889–95. doi: 10.3109/0284186X.2014.958197
8. Kapanen M, Tenhunen M. T1/T2*-Weighted MRI Provides Clinically Relevant pseudo-CT Density Data for the Pelvic Bones in MRI-only Based Radiotherapy Treatment Planning. *Acta Oncol* (2013) 52(3):612–8. doi: 10.3109/0284186X.2012.692883
9. Kapanen M, Collan J, Beule A, Seppala T, Saarihtinen K, Tenhunen M. Commissioning of MRI-only Based Treatment Planning Procedure for External Beam Radiotherapy of Prostate. *Magn Reson Med* (2013) 70(1):127–35. doi: 10.1002/mrm.24459
10. Dowling JA, Sun J, Pichler P, Rivest-Henault D, Ghose D, Richardson H, et al. Automatic Substitute Computed Tomography Generation and Contouring for Magnetic Resonance Imaging (MRI)-Alone External Beam Radiation Therapy From Standard MRI Sequences. *Int J Radiat Oncol Biol Phys* (2015) 93(5):1144–53. doi: 10.1016/j.ijrobp.2015.08.045
11. Johansson A, Karlsson M, Nyholm T. CT Substitute Derived From MRI Sequences With Ultrashort Echo Time. *Med Phys* (2011) 38(5):2708–14. doi: 10.1118/1.3578928
12. Edmund JM, Kjer HM, Leemput KV, Hansen RH, Andersen JA, Andreassen D. A Voxel-Based Investigation for MRI Only Radiotherapy of the Brain Using

- Ultra Short Echo Times. *Phys Med Biol* (2014) 59(23):7501–19. doi: 10.1088/0031-9155/59/23/7501
13. Stanescu T, Jans HS, Pervez N, Stavrev P, Fallone BG. A Study on the Magnetic Resonance Imaging (MRI)-Based Radiation Treatment Planning of Intracranial Lesions. *Phys Med Biol* (2008) 53(13):3579–93. doi: 10.1088/0031-9155/53/13/013
 14. Hsu SH, Cao Y, Huang K, Feng M, Balter JM. Investigation of a Method for Generating Synthetic CT Models From MRI Scans of the Head and Neck for Radiation Therapy. *Phys Med Biol* (2013) 58(23):8419–35. doi: 10.1088/0031-9155/58/23/8419
 15. Kerkhof EM, Balter JM, Vineberg K, Raaymakers BW. Treatment Plan Adaptation for MRI-guided Radiotherapy Using Solely MRI Data: A CT-Based Simulation Study. *Phys Med Biol* (2010) 55(16):N433–40. doi: 10.1088/0031-9155/55/16/N01
 16. Edmund JM, Andreassen D, Mahmood F, Leemput K. Van, Cone Beam Computed Tomography Guided Treatment Delivery and Planning Verification for Magnetic Resonance Imaging Only Radiotherapy of the Brain. *Acta Oncol* (2015) 54(9):1496–500. doi: 10.3109/0284186X.2015.1062546
 17. Lauri K, Leonard W, Juha K. Feasibility of MRI-only Treatment Planning for Proton Therapy in Brain and Prostate Cancer: Dose Calculation Accuracy in Substitute CT Images. *Med Phys* (2016) 43(8):4634–41. doi: 10.1118/1.4958677
 18. Samaneh K, Ana MBM, Kevin S, Sara TR, Robert T, Yang KP, et al. Dosimetric Evaluation of Synthetic CT Generated With GANs for MRI-only Proton Therapy Treatment Planning of Brain Tumors. *Rad Oncol Phys* (2020) 21(5):76–86. doi: 10.1002/acm2.12856
 19. Jinsoo U, Thomas EM, Yimei L, Xingyu L, Chiaho H. MRI-Based Treatment Planning With Pseudo CT Generation Through Atlas Registration. *Med Phys* (2014) 41(5):051711. doi: 10.1118/1.4873315
 20. Han X. MR-Based Synthetic CT Generation Using a Deep Convolutional Neural Network Method. *Med Phys* (2017) 44:1408–19. doi: 10.1002/mp.12155
 21. Jie F, Yingli Y, Kamal S, Dan R, Fang IC, Daniel AL, et al. Deep Learning Approaches Using 2D and 3D Convolutional Neural Networks for Generating Male Pelvic Synthetic Computed Tomography From Magnetic Resonance Imaging. *Med Phys* (2019) 46(9):3788–98. doi: 10.1002/mp.13672
 22. Dinank G, Michelle K, Karen AV, James MB. Generation of Synthetic CT Images From MRI for Treatment Planning and Patient Positioning Using a 3-Channel U-Net Trained on Sagittal Images. *Front Oncol* (2019) 9:964. doi: 10.3389/fonc.2019.00964
 23. Per W, Simon K, Anders E. Generative Adversarial Networks for Image-to-Image Translation on Multi-Contrast MR Images – A Comparison of cycleGAN and UNIT. *Com Vis Patt Recog* (2018) (ArXiv: 1806.07777).
 24. Zhu J-Y, Park T, Isola P, Efros AA. Unpaired Image-to-Image Translation Using Cycle-Consistent Adversarial Networks. *IEEE International Conference on Computer Vision Mar* (2017) 2242–51 (ArXiv:1703.10593). doi: 10.1109/ICCV.2017.244
 25. Liu M-Y, Breuel T, Kautz J. Unsupervised Image-to-Image Translation Networks. *Com Vis Patt Recog* (2017) (ArXiv:1703.00848).
 26. Marques JP, Simonis FFJ, Webb AG. Low-Field MRI: An MR Physics Perspective. *J Magn Reson Imaging* (2019) 49:1528–42. doi: 10.1002/jmri.26637
 27. Sarraçanie M, LaPierre CD, Salameh N, Waddington DEJ, Witzel T, Rosen MS. Low-Cost High-Performance MRI. *Sci Rep* (2015) 5:15177. doi: 10.1038/srep15177
 28. Sheth KN, Mazurek MH, Yuen MM, Cahn BA, Shah JT, Ward A, et al. Assessment of Brain Injury Using Portable, Low-Field Magnetic Resonance Imaging At the Bedside of Critically Ill Patients. *JAMA Neurol* (2020) 8:e203263. doi: 10.1001/jamaneurol.2020.3263
 29. Aganj I, Iglesias JE, Reuter M, Sabuncu MR, Fischl B. Mid-Space-Independent Deformable Image Registration. *NeuroImage* (2017) 152:158–70. doi: 10.1016/j.neuroimage.2017.02.055
 30. Liu M-Y, Breuel T, Kautz J. Unsupervised Image-to-Image Translation Networks. *Com Vis Patt Recog* (2017) (ArXiv:1703.00848) doi: 10.1109/ICCV.2017.244
 31. Choi Y, Choi M, Kim M, Ha J-W, Kim S, Choo J. Stargan: Unified Generative Adversarial Networks for Multi-Domain Image-to-Image Translation. *EEE/CVF Conference on Com Vis Patt Recog* (2018) 8789–97 (ArXiv:1711.09020). doi: 10.1109/CVPR.2018.00916
 32. Zhou S, Xiao T, Yang Y, Feng D, He Q, He W. Genegan: Learning Object Transfiguration and Attribute Subspace From Unpaired Data. *Com Vis Patt Recog* (2017) (ArXiv:1705.04932). doi: 10.5244/C.31.111
 33. Yi Z, Zhang H, Tan P, Gong M. Dualgan: Unsupervised Dual Learning for Image-to-Image Translation. *Com Vis Patt Recog* (2017) (ArXiv:1704.02510). doi: 10.1109/ICCV.2017.310

Conflict of Interest: The authors declare that the research was conducted in the absence of any commercial or financial relationships that could be construed as a potential conflict of interest.

Copyright © 2021 Yoo, Choi, Rah, Lee, Cai, Min and Kim. This is an open-access article distributed under the terms of the Creative Commons Attribution License (CC BY). The use, distribution or reproduction in other forums is permitted, provided the original author(s) and the copyright owner(s) are credited and that the original publication in this journal is cited, in accordance with accepted academic practice. No use, distribution or reproduction is permitted which does not comply with these terms.